

# Coupling Strength and Total Damping Govern Electromagnetically Induced Absorption in Coupled Plasmonic Systems

Kishin Matsumori,\* Ryushi Fujimura, and Markus Retsch

Electromagnetically induced absorption (EIA) is an optical phenomenon that enhances light absorption of plasmonic systems. Depending on the plasmonic system under investigation, the decisive role of intrinsic versus radiative damping and phase retardation has been pointed out to control the EIA. Herein, a unified interpretation is provided and the mechanism of EIA for plasmonic–dielectric composites and all-plasmonic dipolar–quadrupolar antennas is unraveled. In this theoretical work, the finite element method is used to elucidate how EIA is attributed to an absorption enhancement of a resonance mode excited by near-field coupling. For a fundamental understanding, a quantitative analysis is developed by designing an extended coupled-oscillator model. A critical parameter to maximize EIA is found, which is different from previous interpretations of such coupled plasmonic systems. Namely, the ratio of coupling strength to the total damping of the entire system controls EIA. The generalized interpretation of EIA given by this work can be applied to many plasmonic systems and is essential for designing future optical components and devices.

## 1. Introduction

Electromagnetically induced transparency (EIT) is an optical phenomenon occurring as a result of Fano interference.<sup>[1]</sup> EIT can be observed in coupled plasmonic systems composed of bright and dark oscillators. The bright oscillator strongly couples with the incident field but the dark oscillator indirectly couples with an incident field through a near-field coupling to the bright

oscillator. This coupling occurs destructively. Thus, an absorption spectrum is split into two peaks, and a transparency window appears at the resonance of the dark oscillator.<sup>[2]</sup> In the transparency window, a material's dispersion dynamically changes.<sup>[2d,e,3]</sup> These unique optical phenomena have been applied for slow light,<sup>[2e,3,4]</sup> nonlinear optics,<sup>[5]</sup> and sensing.<sup>[6]</sup> Recently, the mode splitting phenomenon of EIT has been utilized to obtain broadband absorption from simpler plasmonic systems.<sup>[7]</sup> The counterpart of EIT is electromagnetically induced absorption (EIA). EIA can also be observed in similar coupled plasmonic systems for EIT. In contrast to EIT, EIA significantly enhances the absorption of the systems at the resonance of the dark oscillator, and the mode splitting is not observed.<sup>[2c,d,8]</sup> EIA has been extensively investigated, and EIA-based plasmonic systems have been

developed for perfect absorbers,<sup>[8c]</sup> optical modulators,<sup>[9]</sup> nonlinear optics,<sup>[10]</sup> and Faraday rotation.<sup>[11]</sup>

The mechanism of EIT is almost the same for any type of plasmonic system; however, the mechanism of EIA is described by different interpretations depending on the coupled plasmonic systems. One interpretation is that EIA is excited by controlling a ratio of radiative to intrinsic damping of the bright oscillator.<sup>[2c]</sup> This interpretation originated from the temporal coupled mode theory, which was used to describe absorption properties of composite systems comprising a plasmonic particle covered with a thin shell with molecular vibrational mode, such as J-aggregate or poly(methyl methacrylate) (PMMA). It is known that the absorption of plasmonic systems is maximized under the condition that its radiative damping equals its intrinsic damping.<sup>[12]</sup> When the LSP of the plasmonic particle couples with the molecular vibration, the total intrinsic damping of the composite system becomes a sum of the intrinsic damping of the LSP and the molecular vibration. Therefore, if the plasmonic particle in the composite system has an intrinsic damping smaller than the radiative damping, the total intrinsic damping of the composite system can be equal to the radiative damping at the resonance of the molecular vibration. This spectrally local increase in the intrinsic damping results in an EIA-like spectral profile. Another interpretation of EIA can be found in a fully plasmonic system: a dipolar antenna vertically stacked over a quadrupolar antenna.<sup>[8a,b]</sup> This system suggested that there is phase

K. Matsumori, M. Retsch  
Department of Chemistry  
Physical Chemistry I  
University of Bayreuth  
Universitätsstraße 30, 95447 Bayreuth, Germany  
E-mail: kishin.matsumori@uni-bayreuth.de

R. Fujimura  
Graduate School of Regional Development and Creativity  
Utsunomiya University  
Utsunomiya 321-8585, Japan

 The ORCID identification number(s) for the author(s) of this article can be found under <https://doi.org/10.1002/adpr.202200211>.

© 2023 The Authors. Advanced Photonics Research published by Wiley-VCH GmbH. This is an open access article under the terms of the Creative Commons Attribution License, which permits use, distribution and reproduction in any medium, provided the original work is properly cited.

DOI: 10.1002/adpr.202200211

retardation in the coupling due to a near- and far-field effect originating from a physical distance between the dipolar and quadrupolar antennas. It was described that this phase retardation can make the coupling destructive or constructive by controlling the distance, and an EIA-like spectral profile can be obtained when the coupling is constructive. Those two distinct interpretations have been utilized to explain EIA occurring in other coupled plasmonic systems.<sup>[8c,11,13]</sup> However, it is still unclear how the ratio of the radiative to the intrinsic damping and the phase retardation in coupling enhance the absorption of those coupled plasmonic systems. In addition to those interpretations, planar plasmonic systems suggested that an absorption of a dark oscillator contributes to EIA.<sup>[2d,14]</sup>

In this work, we integrate the previously established interpretations and develop a fundamental comprehension of EIA by theoretically investigating the absorption properties of the two-representative coupled plasmonic systems mentioned earlier: the plasmonic–polymer antenna (PPA) and the dipolar–quadrupolar antenna (DQA). Using the finite element method (FEM), we find that strong absorption enhancement occurs on the dark oscillator for both systems, which is attributed to the EIA-like spectral profile. To understand how the absorption of the dark oscillator is enhanced, we use a coupled-oscillator (CO) model composed of two mechanical harmonic oscillators coupled via a spring. The CO model has been widely used to investigate the optical properties, especially EIT and EIA properties of plasmonic systems. Depending on which system is investigated, different CO models have been developed.<sup>[2a,b,7b,8,14,15]</sup> In general, those conventional CO models consider only either the intrinsic or radiative damping channels of a system. These CO models are useful to investigate the extinction, scattering, or absorption of the systems individually, but a full description of their optical properties cannot be given. This is because plasmonic structures always contain both intrinsic and radiative damping. As it has been suggested that the system's damping is an essential parameter for plasmonic EIA,<sup>[2c,d]</sup> a CO model must involve all damping channels of the systems to investigate plasmonic EIA. Based on this idea, we design an extended CO (ECO) model involving all intrinsic and radiative damping channels. The radiative damping is given by the Abraham–Lorentz force, which works on charges emitting radiation.<sup>[16]</sup> Throughout this work, we demonstrate that the ECO model quantitatively reproduces not only the absorption but also the scattering spectra obtained from the FEM for both plasmonic systems (PPA and DQA). From the ECO model, we can derive a condition to maximize plasmonic EIA via the absorption of the dark oscillator. Going beyond the established understanding of the role of intrinsic versus radiative damping<sup>[2c]</sup> and phase retardation of the coupling,<sup>[8a,b]</sup> we find that EIA is solely determined by the ratio of the coupling strength to the total damping of the whole system.

## 2. Plasmonic–Polymer Composite Antenna

### 2.1. Design of the PPA and Calculation Method

First, we investigate the optical properties of a plasmonic–polymer composite system. Then, we elucidate how the ratio

of radiative to intrinsic damping of a plasmonic structure influences the mechanism of EIA. For this investigation, we designed the PPA, composed of an Au antenna covered with a PMMA shell (**Figure 1a**). The Au antenna is a cylindrical structure with a radius of  $r$ . The tips of the antenna are spherical with a radius of  $r$ . The tip-to-tip length of the antenna is  $l$ . It is known that the ratio of scattering ( $C_{\text{sca}}$ ) to absorption cross section ( $C_{\text{abs}}$ ) in the Au antenna can be controlled by tuning the aspect ratio of  $r/l$ .<sup>[13,17]</sup>  $C_{\text{sca}}$  and  $C_{\text{abs}}$  are directly related to radiative and intrinsic damping, respectively. Based on this, different ratios of radiative to intrinsic damping can be obtained by controlling  $C_{\text{sca}}/C_{\text{abs}}$ . The PMMA shell with a thickness of  $t$  uniformly covers the Au antenna. PMMA has been widely used to investigate interactions between an LSP and a molecular vibration because PMMA has a strong molecular vibration of C=O stretch at around a wavelength of 5.8  $\mu\text{m}$ .<sup>[2c,18]</sup> If an LSP of the Au antenna is induced at the same wavelength, the LSP of the Au antenna and the molecular vibration of PMMA strongly couple. Therefore, the size of the Au antenna should be determined such that the LSP is induced at around 5.8  $\mu\text{m}$ . The coupling strength between the LSP and the C=O stretch can be changed by changing the thickness. This is because the coupling becomes stronger if more molecules interact with the LSP.<sup>[19]</sup>

The optical properties of the PPA were calculated using COMSOL Multiphysics, which is a commercial software package based on the FEM. The dielectric function of Au was taken from Babar et al.<sup>[20]</sup> For PMMA, the Lorentz model was fitted to the dielectric function of PMMA obtained from Zhang et al.<sup>[21]</sup> From the fitting, the resonance angular frequency and the damping rate of the C=O stretch was  $\omega_{\text{C=O}} = 3.26 \times 10^{14} \text{ rad s}^{-1}$  (5.78  $\mu\text{m}$  in wavelength) and  $\gamma_{\text{C=O}} = 5.3 \times 10^{12} \text{ rad s}^{-1}$ , respectively (see S1, Supporting Information). The refractive index of the surrounding of the PPA was fixed as  $n_{\text{bg}} = 1.46$ , which coincides with the background refractive index of PMMA. This is to prevent a shift of the LSP depending on the thickness of the PMMA shell. An incident field is polarized along the  $x$ -axis and propagates along the  $z$ -axis. A perfectly matched layer (PML) was applied to the surrounding of the calculation domain.  $C_{\text{sca}}$  was calculated by taking the surface integral of the Poynting vector of the scattered field over the integration sphere, which was defined between the structure and the PML.  $C_{\text{abs}}$  was calculated by taking the volume integral of energy dissipation density over the structure. Extinction cross section ( $C_{\text{ext}}$ ) was calculated by  $C_{\text{sca}} + C_{\text{abs}}$ .

### 2.2. Absorption Properties of the PPA

The optical properties of the bare Au antenna with different sizes are shown in the top panels of Figure 1b. We have to mention that the aspect ratios of those Au antennas are very high. Considering the enormous progress in the synthesis of highly anisotropic metallic nanoparticles, however, the investigated aspect ratios fall within a reasonable range.<sup>[22]</sup> The smallest Au antenna has  $C_{\text{sca}}/C_{\text{abs}} < 1$ , the medium one has  $C_{\text{sca}}/C_{\text{abs}} = 1$ , and the biggest one has  $C_{\text{sca}}/C_{\text{abs}} > 1$ . For all sizes, the Au antenna has one LSP mode at around 5.78  $\mu\text{m}$ . The absorption spectra of the PPA with different shell thicknesses are also shown in the top panels of Figure 1b. For the case of

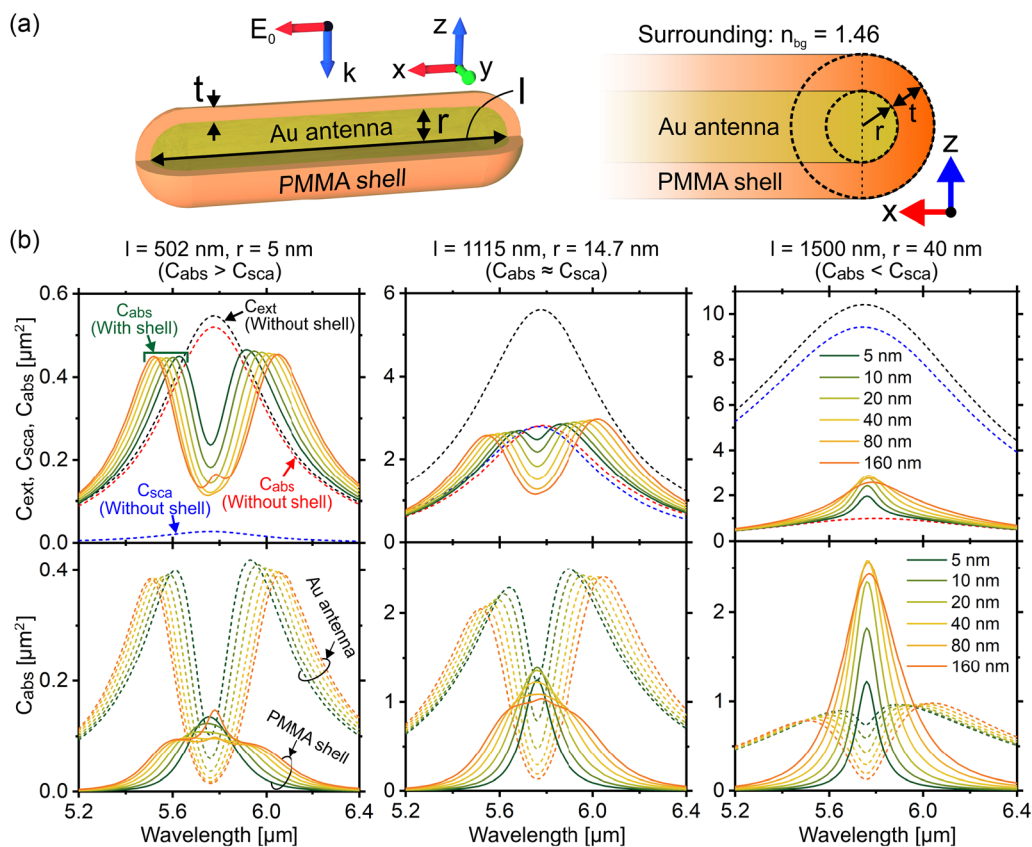


**Figure 1.** a) Schematic illustrations of the PPA. The refractive index of the surrounding is  $n_{bg} = 1.46$ . b) (Top panels) The black, blue, and red dashed lines are the extinction, scattering, and absorption spectra of the Au antenna without the PMMA shell, respectively. The solid lines are the absorption spectra of the PPA. (Bottom panels) The dashed and solid lines show the absorption spectra of the Au antenna and PMMA shell in the PPA, respectively.

$C_{sca}/C_{abs} < 1$  and  $C_{sca}/C_{abs} = 1$ , there are two absorption peaks, and the distance between those two peaks becomes larger with increasing shell thickness. The absorption dip appears at the resonance of the C=O stretch of PMMA, meaning that the LSP of the Au antenna strongly interacts with the C=O stretch. However, for the case of  $C_{sca}/C_{abs} > 1$ , the absorption spectra do not show mode splitting. The absorption is enhanced at the resonance of the C=O stretch, and a sharp absorption peak appears in addition to the broad absorption spectra. This spectral shape has been regarded as EIA.<sup>[2c,13]</sup> The extinction and scattering spectra of the PPA can be found in Figure S2, Supporting Information. In contrast to the absorption, the extinction and scattering spectra show mode splitting no matter how large  $C_{sca}/C_{abs}$  is. The extinction and scattering spectra of the PPA do not have a similar spectral shape to the absorption spectra because the PMMA shell does not strongly scatter the incident field (Figure S3, Supporting Information).

To better understand the absorption properties of the PPA, the absorption of the PPA is divided into the absorption contribution of the Au antenna and PMMA shell (in the bottom panels of Figure 1b). The absorption of the Au antenna splits into two peaks for all antenna sizes and shell thicknesses. On the other hand, the PMMA shell has relatively sharp absorption spectra. This sharp absorption becomes broader with an increase in  $t$ . In general, the C=O stretch cannot strongly couple to the

incident field, so the absorption of the PMMA shell is weak when the PMMA shell is not combined with the Au antenna (Figure S3, Supporting Information). However, in the PPA, the Au antenna creates a strong near-field by its LSP, and the C=O stretch strongly couples with the near-field, resulting in a significant enhancement in the absorption of the PMMA shell (Figure S4, Supporting Information).<sup>[19b,23]</sup> We have to note that for the smallest PPA with a large  $t$ , the PMMA shell has a sharp absorption peak at the resonance of the C=O stretch in addition to the broad absorption spectrum (e.g.,  $l = 502$  nm,  $r = 5$  nm,  $t = 160$  nm). This sharp peak is not attributed to the near-field coupling but is attributed to the intrinsic absorption of the C=O stretch (see S2, Supporting Information).

When  $C_{sca}/C_{abs} \leq 1$ , the absorption of the Au antenna dominates the total absorption of the PPA. As the mode splitting occurs on the LSP of the Au antenna by the near-field coupling, the total absorption of the PPA shows an EIT-like spectral profile. In contrast, for the case of  $C_{sca}/C_{abs} > 1$ , the absorption of the PMMA shell is stronger than that of the Au antenna, resulting in the EIA-like spectral profile of the total absorption of the PPA. These results show that  $C_{sca}/C_{abs}$  of the Au antenna is an important parameter to observe an EIA-like spectral profile, which Adato et al. demonstrated.<sup>[2c]</sup> In addition, our results suggest that the absorption enhancement of the PMMA shell contributes to the EIA-like spectral profile.<sup>[2d,14]</sup> Therefore, one might

understand that the plasmonic EIA of the PPA is maximized when the absorption of the PMMA shell is maximized. However, for all PPA structures investigated here, we observe that the absorption of the PMMA shell increases, is maximized at a certain  $t$ , and becomes broader. This result indicates that there is a condition of maximum absorption of the PMMA shell, which is independent of  $C_{sca}/C_{abs}$  of the Au antenna. As the shell thickness determines the coupling strength, the coupling strength may play a key role in the maximum absorption of the PMMA shell. In the following, we will discuss how the maximum absorption of the PMMA shell and  $C_{sca}/C_{abs}$  of the Au antenna are relevant to plasmonic EIA.

### 2.3. An Extended CO Model

We propose an ECO model that involves all damping channels of the PPA system, which enables us to investigate the mechanism of plasmonic EIA in this case (see Figure 2a).<sup>[2c,d]</sup> This model extends the understanding of EIA beyond the established interpretation based on intrinsic versus radiative damping. Our ECO model consists of two harmonic oscillators. One is a bright oscillator driven by an external force. Another is a dark oscillator connected to the bright oscillator by a spring, which describes the near-field coupling of the system. Comparing the ECO model and the PPA, the bright and dark oscillators correspond to the

Au antenna and the PMMA shell, respectively. The equations of motion of the ECO model can be written as

$$\frac{d^2 x_{B\alpha}}{dt^2} + \gamma_B \frac{dx_{B\alpha}}{dt} + \omega_B^2 x_{B\alpha} - \kappa^2 x_{D\alpha} = F(t) + \tau_B \frac{d^3 x_{B\alpha}}{dt^3} \quad (1)$$

$$\frac{d^2 x_{D\alpha}}{dt^2} + \gamma_D \frac{dx_{D\alpha}}{dt} + \omega_D^2 x_{D\alpha} - \kappa^2 x_{B\alpha} = 0 \quad (2)$$

The subscripts  $n = B$  and  $D$  represent the bright and dark oscillators, respectively. The subscript  $\alpha$  distinguishes Equations (1) and (2) from another ECO model that will be shown later.  $x_n$  is the displacement of the mass objects.  $\gamma_n$  is the intrinsic damping rate,  $\omega_n$  is the resonance angular frequency determined by the spring constant, and  $\kappa$  is the coupling rate.  $\tau_n$  is the radiative damping coefficient given by the Abraham–Lorentz force,<sup>[16]</sup> and the radiative damping rate is expressed as  $\tau_n \omega^2$ . The total damping of the oscillator is  $\Gamma_n = \gamma_n + \tau_n \omega^2$ .  $F(t)$  is the external force normalized by the mass  $m_B$ , which is time-harmonic; therefore,  $F(t) = F_0 e^{-i\omega t}$ . In Equation (2), a radiative damping term is not included because the radiative damping of the PMMA shell is negligibly small (Figure S3, Supporting Information). In addition, Equation (2) does not have an external force term. This is attributed to the fact that, in our case, the excitation of the PMMA shell is dominated by the near-field coupling (Figure S4, Supporting

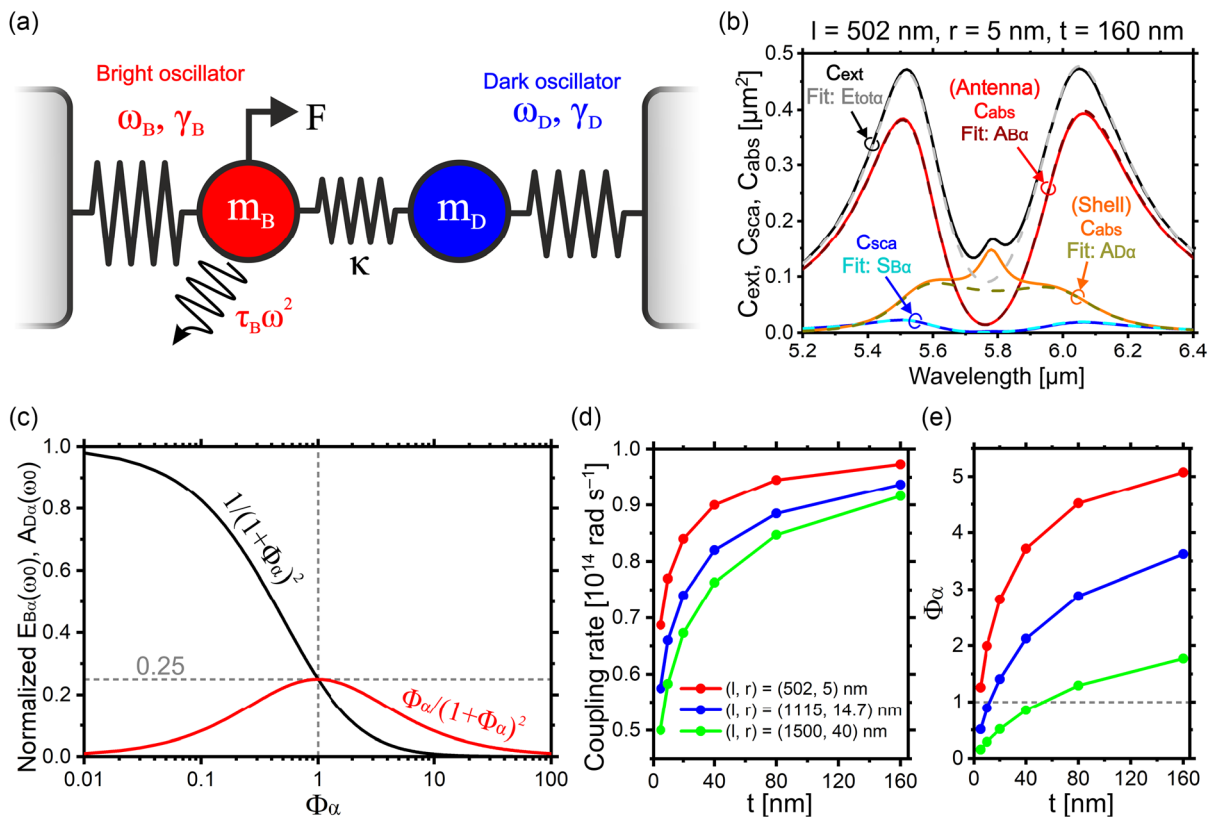


**Figure 2.** a) Schematic illustration of the ECO model. b) Optical cross-sectional spectra of the PPA. The black and blue solid lines are the extinction and scattering spectra of the whole system, respectively. The red and orange solid lines are the absorption spectra of the Au antenna and the PMMA shell, respectively. The dashed lines are calculated using the ECO model (Equation (4)) and fitted to the solid lines. c)  $E_{B\alpha}(\omega_0)$  and  $A_{D\alpha}(\omega_0)$  normalized by  $F_0^2/(2\Gamma_{B\alpha})$ . d) The coupling rate and e)  $\Phi_\alpha$  of the PPA as a function of the shell thickness  $t$ .

Information). We must note that an external force term may need to be included in Equation (2) if a different polymer shell and antenna are used in the PPA system (a description can be found in S2, Supporting Information). The time-averaged dissipated power of the whole system is

$$P = \left\langle \text{Re} \left[ F^*(t) \times \frac{dx_B}{dt} \right] \right\rangle \quad (3)$$

The dissipated power of the system described by Equations (1) and (2) can be written as<sup>[16a]</sup>

$$P_\alpha = \frac{1}{2} (\gamma_B \omega^2 |x_{B\alpha}|^2 + \tau_B \omega^4 |x_{B\alpha}|^2 + \gamma_D \omega^2 |x_{D\alpha}|^2) = E_{\text{tot}\alpha} \\ = A_{B\alpha} + S_{B\alpha} + A_{D\alpha} \quad (4)$$

The absolute squares of  $x_{B\alpha}$  and  $x_{D\alpha}$  are

$$|x_{B\alpha}|^2 = \frac{(\Omega_D^2 + \gamma_D^2 \omega^2) F_0^2}{(\Omega_B \Omega_D - \Gamma_B \gamma_D \omega^2 - \kappa^4)^2 + \omega^2 (\Gamma_B \Omega_D + \gamma_D \Omega_B)^2} \quad (5)$$

$$|x_{D\alpha}|^2 = \frac{\kappa^4 F_0^2}{(\Omega_B \Omega_D - \Gamma_B \gamma_D \omega^2 - \kappa^4)^2 + \omega^2 (\Gamma_B \Omega_D + \gamma_D \Omega_B)^2} \quad (6)$$

where  $\Omega_n = (\omega_n^2 - \omega^2)$ .  $A_{B\alpha}$ ,  $S_{B\alpha}$ , and  $A_{D\alpha}$  correspond to absorption and scattering of the bright oscillator and absorption of the dark oscillator, respectively.  $E_{\text{tot}\alpha}$  is the extinction of the whole system.  $E_{B\alpha} = A_{B\alpha} + S_{B\alpha}$  and  $A_{\text{tot}\alpha} = A_{B\alpha} + A_{D\alpha}$  can be considered the extinction of the bright oscillator and the absorption of the whole system, respectively. To figure out whether the ECO model can explain the optical properties of the PPA, Equation (4) is fitted to optical cross sections of the PPA calculated using the FEM simulation. Before fitting Equation (4), the physical constants of the ECO model have to be extracted. To extract  $F_0$ ,  $\omega_B$ ,  $\gamma_B$ , and  $\tau_B$ , a single harmonic oscillator model is fitted to optical cross sections of the bare Au antennas (Figure S5, Supporting Information), whose results are summarized in Table 1.  $\omega_D$  and  $\gamma_D$  are already known from the optical properties of the C=O stretch of PMMA ( $\omega_D = \omega_{\text{C=O}} = 3.26 \times 10^{14} \text{ rad s}^{-1}$  and  $\gamma_D = \gamma_{\text{C=O}} = 5.3 \times 10^{12} \text{ rad s}^{-1}$ ). Therefore, the coupling rate  $\kappa$  is used as a parameter to fit the ECO model to the FEM simulation. An example of the spectra calculated using the ECO model is shown in Figure 2b, and it can be confirmed that the ECO model nearly perfectly fits the spectra of the FEM simulation. The same fitting result can be obtained for all sizes of the PPA for any  $t$  (Figure S6a, Supporting Information). This result proves that the ECO model is an appropriate quantitative model to describe

**Table 1.**  $\omega_B$ ,  $\gamma_B$ , and  $\tau_B$  of the bare Au antennas.

$(l, r)$ [nm] <sup>a)</sup>	$\omega_B$ [ $10^{14} \text{ rad s}^{-1}$ ]	$\gamma_B$ [ $10^{13} \text{ rad s}^{-1}$ ]	$\tau_B \omega_B^2$ [ $10^{13} \text{ rad s}^{-1}$ ]
(502, 5)	3.26	2.95	0.16
(1115, 14.7)	3.27	1.88	1.87
(1500, 40)	3.31	0.65	6.35

<sup>a)</sup> Those values were obtained by fitting a single harmonic oscillator model to the optical cross sections of the bare Au antenna (see S2, Supporting Information).

the optical properties of the PPA. Note that there is a discrepancy between the ECO model and the FEM simulation for the PMMA shell's absorption at around the resonance of the C=O stretch. This discrepancy is attributed to the intrinsic absorption of PMMA. Our ECO model only considers the near-field coupling effect but does not take this intrinsic absorption into account (Figure S6b, Supporting Information).

As mentioned earlier, the absorption of the PMMA shell is strongly enhanced by the coupling between the LSP of the Au antenna and the C=O stretch of PMMA, and the absorption is maximized at a certain shell thickness. Using our ECO model, we find a condition to maximize the absorption of the PMMA shell. Considering that the absorption of the PMMA shell is enhanced at the resonance of the C=O stretch, the ECO model has to be solved at  $\omega_D$ . From the fitting shown in Table 1, it is known that the resonance frequency of the LSP of the Au antenna is almost the same as that of the C=O stretch of PMMA, meaning that  $\omega_B = \omega_D$ . Therefore,  $E_{B\alpha}$  and  $A_{D\alpha}$  at the resonance ( $\omega = \omega_0 = \omega_B = \omega_D$ ) can be written as

$$E_{B\alpha}(\omega_0) = \frac{1}{\Gamma_{B\alpha}} \frac{1}{(1 + \Phi_\alpha)^2} \frac{F_0^2}{2} \quad (7)$$

$$A_{D\alpha}(\omega_0) = \frac{1}{\Gamma_{B\alpha}} \frac{\Phi_\alpha}{(1 + \Phi_\alpha)^2} \frac{F_0^2}{2} \quad (8)$$

where  $\Phi_\alpha = \kappa^4 / (\Gamma_{B\alpha} \gamma_D \omega_0^2)$  and  $\Gamma_{B\alpha} = \gamma_B + \tau_B \omega_0^2$ .  $\Phi_\alpha$  describes the ratio of the coupling rate to the total damping of the whole system. From Equation (7), it can be found that  $E_{B\alpha}(\omega_0)$  is maximized when there is no coupling between the bright and dark oscillators, meaning  $\Phi_\alpha = 0$ . Therefore, the maximum of  $E_{B\alpha}(\omega_0)$  can be expressed as  $F_0^2 / (2\Gamma_{B\alpha})$ . By normalizing  $E_{B\alpha}(\omega_0)$  and  $A_{D\alpha}(\omega_0)$  with  $F_0^2 / (2\Gamma_{B\alpha})$ ,  $E_{B\alpha}(\omega_0)$  and  $A_{D\alpha}(\omega_0)$  can be expressed only as a function of  $\Phi_\alpha$ . In Figure 2c, the normalized  $E_{B\alpha}(\omega_0)$  and  $A_{D\alpha}(\omega_0)$  are shown.  $E_{B\alpha}(\omega_0)$  keeps decreasing with an increase in  $\Phi_\alpha$ . In contrast,  $A_{D\alpha}(\omega_0)$  increases with increasing  $\Phi_\alpha$ , is maximized at  $\Phi_\alpha = 1$ , and starts decreasing with further increase in  $\Phi_\alpha$ . Therefore, we can find that  $\Phi_\alpha = 1$  is the condition for maximum absorption of the PMMA shell. We call this condition critical coupling. The critical coupling means that energy transferred between the bright and dark oscillators takes balance with the energy dissipated by the whole system.<sup>[19b,23,24]</sup> From Figure 2c, it is found that the maximum value of the normalized  $A_{D\alpha}(\omega_0)$  is 0.25. This result indicates that the absorption of the PMMA shell can be maximized up to 25% of the maximum of the extinction of the Au antenna.

To calculate  $\Phi_\alpha$  for the PPA, the coupling rate of the PPA must be known. The coupling rates obtained from the fitting are shown in Figure 2d. The coupling rate is determined by the amplitude of the near-field created by the Au antenna. As a smaller antenna has a lower radiative damping rate, the smaller antenna can create a stronger near-field (Figure S4, Supporting Information),<sup>[25]</sup> resulting in a higher coupling rate.<sup>[19b,26]</sup> In addition, as mentioned earlier, the coupling rate is influenced by the number of molecules interacting with the LSP of the Au antenna. The number of interacting molecules increases with an increase in the shell thickness of the PMMA shell. Therefore, the coupling rate is higher for thicker shell thickness. Using the values in Table 1 and the coupling rate in Figure 2d,  $\Phi_\alpha$  is

calculated as a function of the shell thickness (Figure 2e).  $\Phi_\alpha$  shows a similar trend as the coupling rate because all values in  $\Phi_\alpha$  except  $\kappa$  are constant. For the smallest, medium, and largest PPAs, the critical coupling ( $\Phi_\alpha = 1$ ) is nearly satisfied at  $t = 5, 10,$  and  $40$  nm, respectively. In Figure 1b, we can see that the absorption of the PMMA shell is maximized at those shell thicknesses. This result demonstrates that the condition for the maximum absorption of the PMMA shell can be found from  $\Phi_\alpha$ . As described earlier,  $\Phi_\alpha$  comprises the coupling rate and the damping rate of the whole system. In consequence,  $C_{\text{sca}}/C_{\text{abs}}$  of the Au antenna, which directly correlates the ratio of radiative to intrinsic damping  $q = \tau_B \omega_0^2 / \gamma_B$ , is not a key parameter for the maximum absorption of the PMMA shell.

We make a systematic analysis to gain an insight into the mechanism of the absorption enhancement in the PMMA shell of the PPA.  $E_{B\alpha}$  and  $A_{D\alpha}$  normalized by  $F_0^2 / (2\Gamma_{B\alpha})$  are plotted as functions of the wavelength and  $\Phi_\alpha$  (Figure 3a). For this plot,  $\omega_0 = \omega_B = \omega_D = 3.27 \times 10^{14} \text{ rad s}^{-1}$  and  $\gamma_D = 5.3 \times 10^{12} \text{ rad s}^{-1}$  are used. As can be seen in Equations (4-6), neither  $E_{B\alpha}$  nor  $A_{D\alpha}$  depends on  $q$ . Therefore, for the bright oscillator, the total damping rate is only considered by setting  $\Gamma_{B\alpha} = 3.76 \times 10^{13} \text{ rad s}^{-1}$  ( $\gamma_B$  and  $\tau_B$  are arbitrary values but determined from  $\gamma_B + \tau_B \omega_0^2 = 3.76 \times 10^{13} \text{ rad s}^{-1}$ ).  $\kappa$  is changed so that  $\Phi_\alpha$  can be in a range from 0.1 to 10. In Figure 3a,  $E_{B\alpha}$  shows mode splitting, which becomes stronger with an increase in  $\Phi_\alpha$ . Therefore,  $E_{B\alpha}$  keeps decreasing at the resonance with an increase in  $\Phi_\alpha$  (see Figure 2c). For  $A_{D\alpha}$ , the peak becomes pronounced with an increase in  $\Phi_\alpha$  up to 1. With an increase in  $\Phi_\alpha$  beyond 1,  $A_{D\alpha}$  becomes broader and weaker. This is because the mode splitting starts occurring at the resonance of the dark

oscillator when  $\Phi_\alpha > 1$ , which describes the decrease in  $A_{D\alpha}(\omega_0)$  shown in Figure 2c. As the dark oscillator shows mode splitting only when the coupling is strong,<sup>[23,24,27]</sup> the coupling can be divided into two regimes according to  $\Phi_\alpha$ : 1) When  $\Phi_\alpha < 1$ , the coupling is in a weak coupling regime. In this regime, the energy transferred between the bright and dark oscillators is mostly dissipated in the system. 2) When  $\Phi_\alpha > 1$ , the coupling can be classified into a strong coupling regime because the energy is transferred between the bright and dark oscillators before the energy is dissipated by the system's damping. By having a closer look at the absorption of the dark oscillator, we may obtain more detailed information about the coupling regime (S3, Supporting Information). We appreciate that other groups categorize coupling regimes differently. For example, it has been suggested that the strong coupling is given by  $\kappa \gg (\Gamma_{B\alpha} \gamma_D)^{1/2}$ .<sup>[19b,28]</sup> As demonstrated in Figure 3a,  $\Phi_\alpha$  can give a clear boundary between weak and strong coupling regimes. Therefore,  $\Phi_\alpha$  may be used as an alternative indicator to find those coupling regimes.

Based on the finding from Figure 3a, the absorption properties of the PMMA shell shown in Figure 1b are considered more in detail. In Figure 2e, we demonstrated that the smallest PPA has  $\Phi_\alpha$  larger than 1 for all  $t$ . Therefore, the absorption of the PMMA shell keeps decreasing, and the absorption peak starts splitting into two peaks with an increase in  $t$ . In contrast,  $\Phi_\alpha$  of the medium and the largest PPA cross over 1 with an increase in  $t$ . For those two PPAs, the absorption of the PMMA shell becomes stronger until  $t$  reaches  $\Phi_\alpha = 1$ , and the absorption becomes weaker and broader when  $\Phi_\alpha$  is over 1.

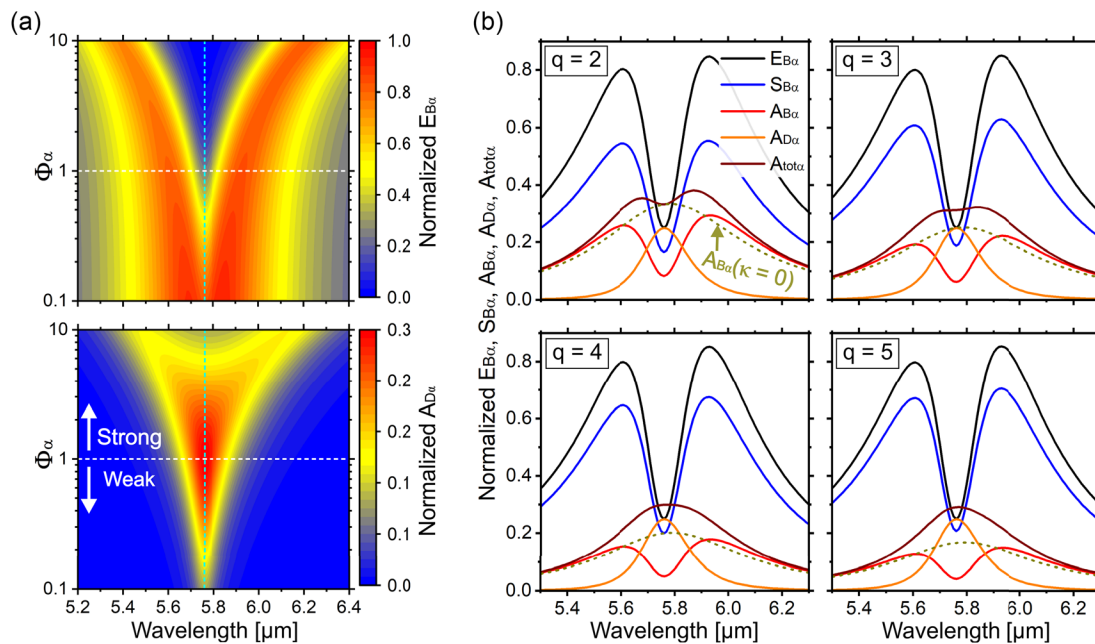


**Figure 3.** a) Color maps of  $E_{B\alpha}$  and  $A_{D\alpha}$  normalized by  $F_0^2 / (2\Gamma_{B\alpha})$ .  $\omega_0 = \omega_B = \omega_D = 3.27 \times 10^{14} \text{ rad s}^{-1}$ ,  $\Gamma_{B\alpha} = 3.76 \times 10^{13} \text{ rad s}^{-1}$ , and  $\gamma_D = 5.3 \times 10^{12} \text{ rad s}^{-1}$  are used.  $q$  is not considered. The white dashed line indicates  $\Phi_\alpha = 1$ . The cyan dashed line indicates  $\omega_0$ . b) The black, blue, red, orange, and wine-red solid lines are  $E_{B\alpha}$ ,  $S_{B\alpha}$ ,  $A_{B\alpha}$ ,  $A_{D\alpha}$ , and  $A_{\text{tot}\alpha}$  normalized by  $F_0^2 / (2\Gamma_{B\alpha})$ . Those are calculated at  $\Phi_\alpha = 1$  in (a) for different  $q = \tau_B \omega_0^2 / \gamma_B$ . As  $\Gamma_{B\alpha}$  is fixed,  $E_{B\alpha}$  and  $A_{D\alpha}$  are nearly identical for all  $q$ . The dark-yellow dashed lines are  $A_{B\alpha}$  without coupling between the bright and the dark oscillators ( $\kappa = 0$ ).

Having addressed the role of critical coupling in the PPA, we finally turn our focus on the influence of  $q = \tau_B \omega_0^2 / \gamma_B$  on the plasmonic EIA.<sup>[2c]</sup> Figure 3b shows  $E_{B\alpha}$ ,  $S_{B\alpha}$ ,  $A_{B\alpha}$ ,  $A_{D\alpha}$ , and  $A_{\text{tot}\alpha}$  calculated at  $\Phi_\alpha = 1$  in Figure 3a. For those spectra,  $q$  is changed so that the total damping is fixed as  $\Gamma_{B\alpha} = 3.76 \times 10^{13} \text{ rad s}^{-1}$ . As mentioned earlier,  $E_{B\alpha}$  and  $A_{D\alpha}$  are independent of  $q$ . Thus,  $E_{B\alpha}$  and  $A_{D\alpha}$  are almost identical for all  $q$ . As all spectra in Figure 3b satisfy  $\Phi_\alpha = 1$ ,  $A_{D\alpha}$  is maximized. With an increase in  $q$ ,  $S_{B\alpha}$  increases,  $A_{B\alpha}$  decreases, and  $A_{\text{tot}\alpha}$  changes from an EIT-like (two peaks) to an EIA-like profile (one pronounced peak). This spectral change of  $A_{\text{tot}\alpha}$  is because two peaks of  $A_{B\alpha}$  are higher than the peak of  $A_{D\alpha}$  when  $q$  is small, but the peak of  $A_{D\alpha}$  can be higher than those two peaks of  $A_{B\alpha}$  when  $q$  is large. Therefore, we derive that  $q$  determines whether  $A_{\text{tot}\alpha}$  possesses an EIT- or EIA-like spectral profile. To observe the EIA-like profile,  $A_{D\alpha} > A_{B\alpha}$  has to be satisfied. This condition may be found by comparing the maximum of  $A_{D\alpha}$  and the maximum of  $A_{B\alpha}$  without coupling (dark yellow dashed lines in Figure 3b), which are  $A_{D\alpha(\text{max})} = (1/4)[F_0^2 / (2\Gamma_{B\alpha})]$  and  $A_{B\alpha(\text{max})} = (\gamma_B / \Gamma_{B\alpha})[F_0^2 / (2\Gamma_{B\alpha})]$ . From those equations,  $A_{D\alpha(\text{max})} > A_{B\alpha(\text{max})}$  can be obtained by  $q > 3$ . In general, when the absorption properties of coupled plasmonic systems are investigated, the total absorption of the system (corresponding to  $A_{\text{tot}\alpha}$ ) is considered. Thus, the plasmonic EIA has been recognized as the absorption spectral shape of  $A_{\text{tot}\alpha}$  that can be seen in Figure 3b for  $q = 4$  and 5. In this case,  $q$  plays a key role in EIA, and the condition for EIA may be found as  $q > 3$ . However, no matter how large  $q$  is,  $A_{D\alpha}$  maximizes when the critical coupling condition is satisfied. Therefore, as EIA and the absorption of the dark oscillator are linked via  $\Phi_\alpha$ , the EIA has to be optimized based on  $\Phi_\alpha$ , not on  $q$ .

### 3. Dipolar–Quadrupolar Antenna

#### 3.1. Design of the DQA and Calculation Method

Next, we focus on EIA occurring in the DQA composed of Au (Figure 4a). To excite EIA, the incident field should propagate along the  $z$ -direction with  $x$ -polarization (parallel to the long axis of the dipolar antenna). In this configuration of the incident field, only the dipolar antenna can strongly couple with the incident field, and the quadrupolar antenna interacts with the dipolar antenna through the near-field created by the dipolar antenna. In the DQA, the near-field coupling is maximized when the dipolar antenna is close to the tip of the quadrupolar antenna. As mentioned earlier, it was suggested that EIA of this fully plasmonic system is induced by the phase retardation in the coupling between the dipolar and quadrupolar antennas. This phase retardation is attributed to the fact that there is a distance between the dipolar and quadrupolar antennas in the  $z$ -direction.<sup>[8a,b]</sup>

To elucidate the mechanism of EIA of the DQA in more detail, we obtained the absorption properties of the DQA using the FEM simulation. The size of the DQA was based on the works of Taubert et al. ( $L_1 = 375 \text{ nm}$ ,  $W_1 = 60 \text{ nm}$ ,  $H_1 = 40 \text{ nm}$ ,  $L_2 = 420 \text{ nm}$ ,  $W_2 = 120 \text{ nm}$ ,  $H_2 = 60 \text{ nm}$ ,  $g = 220 \text{ nm}$ , and the periodicity in the  $x$ - and  $y$ -directions is  $700 \text{ nm}$ ).<sup>[8a,b]</sup> The dielectric function of Au was taken from Rakic et al.<sup>[29]</sup> The surrounding was set as air. As the periodic structure was considered, the Bloch–Floquet periodic boundary conditions were applied in the  $x$ - and  $y$ -directions. PMLs were applied on the top and bottom of the simulation model in the  $z$ -direction. Absorbance was calculated by taking a volume integral of dissipated energy density over the structures and dividing the dissipated energy by the energy of the incident wave per area of the unit cell.

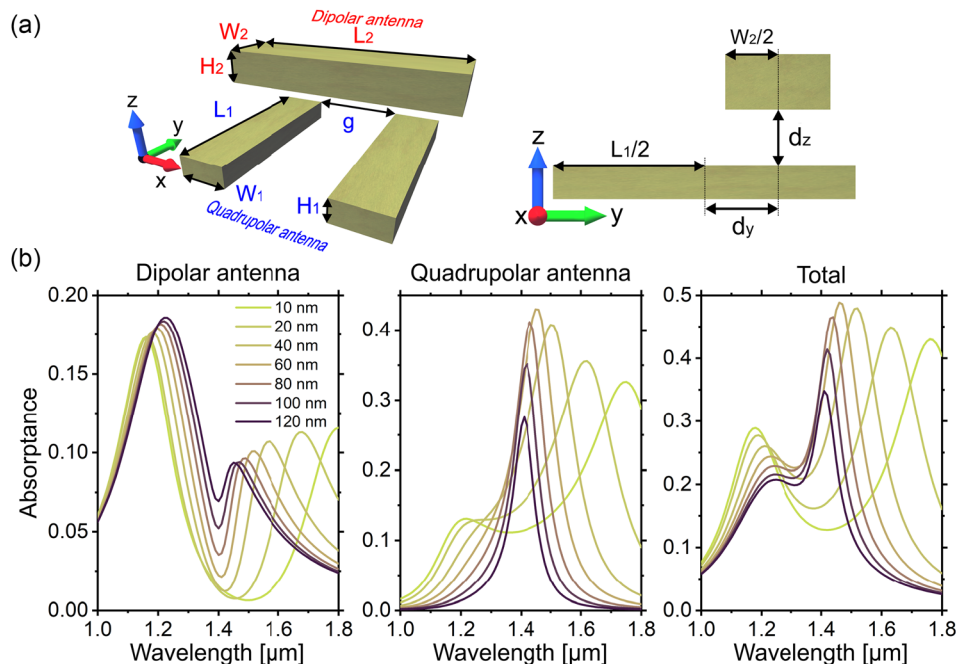


**Figure 4.** a) Schematic illustrations of the DQA. The structural parameters are  $L_1 = 375 \text{ nm}$ ,  $W_1 = 60 \text{ nm}$ ,  $H_1 = 40 \text{ nm}$ ,  $L_2 = 420 \text{ nm}$ ,  $W_2 = 120 \text{ nm}$ ,  $H_2 = 60 \text{ nm}$ , and  $g = 220 \text{ nm}$ . The periodicity in the  $x$ - and  $y$ -directions is  $700 \text{ nm}$ . b) Absorption spectra of the dipolar and the quadrupolar antennas in the DQA, and total absorption spectra of the DQA.  $d_y$  is fixed at  $120 \text{ nm}$ .  $d_z$  is varied in a range of  $10$ – $120 \text{ nm}$ .

### 3.2. Absorption Properties of the DQA

Figure 4b shows absorption spectra of the dipolar antenna, quadrupolar antenna, and DQA for different  $d_z$ .  $d_y$  is fixed at 120 nm. The absorption of the dipolar antenna shows mode splitting for all  $d_z$ . Even though the quadrupolar antenna is considered to be the dark oscillator, it possesses strong absorption. This is because the LSP of the quadrupolar antenna is excited by an indirect path through near-field coupling: incident wave  $\rightarrow$  dipolar oscillator  $\rightarrow$  quadrupolar oscillator. During this indirect excitation process, the incident wave's energy concentrated on the dipolar oscillator is transferred to the quadrupolar oscillator. Part of the transferred energy is absorbed by the LSP of the quadrupolar oscillator. This absorption process is the same as the PMMA shell of the PPA. In contrast to the dipolar antenna, the absorption spectral shape of the quadrupolar antenna dramatically changes with a decrease in  $d_z$ : the absorption has one sharp peak for a large  $d_z$ , it is maximized at a certain  $d_z$ , and it splits into two peaks for a small  $d_z$ . The absorption of the quadrupolar antenna is stronger than that of the dipolar antenna. Therefore, the total absorption of the DQA shows the EIA-like or the EIT-like spectral shape depending on  $d_z$ . These absorption properties of the DQA are similar to those of the PPA discussed earlier.

To gain a deeper insight into the absorption mechanism of the DQA, we again use the ECO model. In the ECO model, the dipolar and quadrupolar antennas correspond to the bright and dark oscillators, respectively. In general, the radiative damping of the quadrupolar antenna is ignored because it is expected that the scattering of the quadrupolar antenna is negligible.<sup>[2b,24]</sup> However, for an accurate quantitative analysis, we introduce the radiative damping of the quadrupolar antenna in the ECO model by adding  $\tau_D$  on the dark oscillator. Therefore, the equations of motion of the ECO model for the DQA are

$$\frac{d^2 x_{B\beta}}{dt^2} + \gamma_B \frac{dx_{B\beta}}{dt} + \omega_B^2 x_{B\beta} - \kappa^2 x_{D\beta} = F(t) + \tau_B \frac{d^3 x_{B\beta}}{dt^3} \quad (9)$$

$$\frac{d^2 x_{D\beta}}{dt^2} + \gamma_D \frac{dx_{D\beta}}{dt} + \omega_D^2 x_{D\beta} - \kappa^2 x_{B\beta} = \tau_D \frac{d^3 x_{D\beta}}{dt^3} \quad (10)$$

The subscript  $\beta$  distinguishes the ECO model of the DQA from that of the PPA. Using Equation (3), (9), and (10), the time-averaged dissipated power of the whole system is given as

$$P_\beta = \frac{1}{2} (\gamma_B \omega^2 |x_{B\beta}|^2 + \tau_B \omega^4 |x_{B\beta}|^2 + \gamma_D \omega^2 |x_{D\beta}|^2 + \tau_D \omega^4 |x_{D\beta}|^2) \quad (11)$$

$$= E_{\text{tot}\beta} = A_{B\beta} + S_{B\beta} + A_{D\beta} + S_{D\beta}$$

where the absolute squares of  $x_{B\beta}$  and  $x_{D\beta}$  are

$$|x_{B\beta}|^2 = \frac{(\Omega_D^2 + \Gamma_D^2 \omega^2) F_0^2}{(\Omega_B \Omega_D - \Gamma_B \Gamma_D \omega^2 - \kappa^4)^2 + \omega^2 (\Gamma_B \Omega_D + \Gamma_D \Omega_B)^2} \quad (12)$$

$$|x_{D\beta}|^2 = \frac{\kappa^4 F_0^2}{(\Omega_B \Omega_D - \Gamma_B \Gamma_D \omega^2 - \kappa^4)^2 + \omega^2 (\Gamma_B \Omega_D + \Gamma_D \Omega_B)^2} \quad (13)$$

Compared to Equation (4), (11) has an additional term  $S_{D\beta}$ , which corresponds to the scattering of the dark oscillator. Therefore,  $E_{D\beta} = A_{D\beta} + S_{D\beta}$  and  $S_{\text{tot}\beta} = S_{B\beta} + S_{D\beta}$  can be considered the extinction of the dark oscillator and

scattering of the whole system, respectively. To figure out whether the ECO model can describe the absorption properties of the DQA,  $A_{B\beta}$ ,  $A_{D\beta}$ , and  $A_{\text{tot}\beta}$  were fitted to the absorption spectra of the dipolar antenna, quadrupolar antenna, and DQA, respectively. Before fitting the ECO model,  $F_0$ ,  $\omega_B$ ,  $\gamma_B$ , and  $\tau_B$  of the dipolar antenna without quadrupolar antenna were extracted by using the single oscillator model, resulting in  $\omega_B = 1.55 \times 10^{15} \text{ rad s}^{-1}$  (1.22  $\mu\text{m}$  in wavelength),  $\gamma_B = 5.23 \times 10^{13} \text{ rad s}^{-1}$ , and  $\tau_B \omega_B^2 = 4.47 \times 10^{14} \text{ rad s}^{-1}$  (S4, Supporting Information). In contrast to the case of the PPA, the ECO model was fitted using all variables as fitting parameters. This fitting was made by referring to the extracted  $F_0$ ,  $\omega_B$ ,  $\gamma_B$ , and  $\tau_B$ . **Figure 5a** shows examples of the fitted  $A_{B\beta}$ ,  $A_{D\beta}$ , and  $A_{\text{tot}\beta}$ . For all  $d_z$ , the ECO model shows good agreement not only for the total absorption of the DQA but also for the absorption of the dipolar and quadrupolar antennas. This result proves that the ECO model is an appropriate quantitative model to describe the absorption properties of the DQA. Note that this nearly perfect fitting cannot be achieved if  $\tau_D = 0$  (S5, Supporting Information). From the fitting, we find that the coupling rate increases, and the resonance wavelength of the quadrupolar antenna ( $\lambda_D = 2\pi c/\omega_D$ , where  $c$  is the speed of light in vacuum) redshifts with decreasing  $d_z$  (Figure 5b). The resonance wavelength of the dipolar antenna also slightly redshifts in a range of 1.22–1.25  $\mu\text{m}$  with decreasing  $d_z$  (Figure S8b, Supporting Information).

In a similar manner to the case of the PPA, the condition for the maximum absorption of the quadrupolar antenna is found using the ECO model. As the absorption of the quadrupolar antenna is enhanced at  $\omega_D$  (see Figure 4b), Equation (11) should be solved at  $\omega = \omega_D$ . However, in the case of the DQA,  $\omega_B$  and  $\omega_D$  are not aligned. Therefore, it is considered that  $\omega_B$  is shifted from  $\omega_D$  by an amount of  $\delta$ . Using  $\omega_B = \omega_D + \delta$ ,  $E_{B\beta}$  and  $E_{D\beta}$  at  $\omega_D$  can be written as

$$E_{B\beta}(\omega_D) = \frac{1}{\Gamma_{B\beta}} \frac{1}{(1 + \Phi_\beta)^2 + \Delta} \frac{F_0^2}{2} \quad (14)$$

$$E_{D\beta}(\omega_D) = \frac{1}{\Gamma_{B\beta}} \frac{\Phi_\beta}{(1 + \Phi_\beta)^2 + \Delta} \frac{F_0^2}{2} \quad (15)$$

where  $\Phi_\beta = \kappa^4 / (\Gamma_{B\beta} \Gamma_{D\beta} \omega_D^2)$ ,  $\Gamma_{n\beta} = \gamma_n + \tau_n \omega_D^2$ , and  $\Delta = \delta^2 [(2\omega_D + \delta) / (\Gamma_{B\beta} \omega_D)]^2$ . For  $\Delta \neq 0$ ,  $E_{D\beta}(\omega_D)$  is maximized when  $\Phi_\beta$  equals  $\Phi_{cc} = (1 + \Delta)^{1/2}$ , which is the critical coupling condition when  $\omega_B \neq \omega_D$ . This critical coupling condition can be applied to  $A_{D\beta}$  because  $A_{D\beta}$  at  $\omega_D$  can be written as  $(\gamma_{Da} / \Gamma_{D\beta}) \times E_{D\beta}(\omega_D)$ . To calculate  $\Phi_\beta$  and  $\Phi_{cc}$  of the DQA, the damping rates at  $\omega_D$  have to be known (Figure 5c). Compared to the intrinsic damping rates, the radiative damping rates dramatically change with a decrease in  $d_z$  for both the dipolar and quadrupolar antennas, resulting in the total damping rate of the quadrupolar antenna exceeding that of the dipolar antenna at  $d_z = 10 \text{ nm}$ . However, when the absorption properties of a single particle of the DQA are investigated, these dramatic changes in the radiative damping rates are not observed (S5, Supporting Information). As the absorption properties of the periodic structure are considered in Figure 4b, near-field interactions occur in lateral directions, which may influence the radiative damping rates.  $\Phi_\beta$  and  $\Phi_{cc}$  calculated using the values in Figure 5b,c

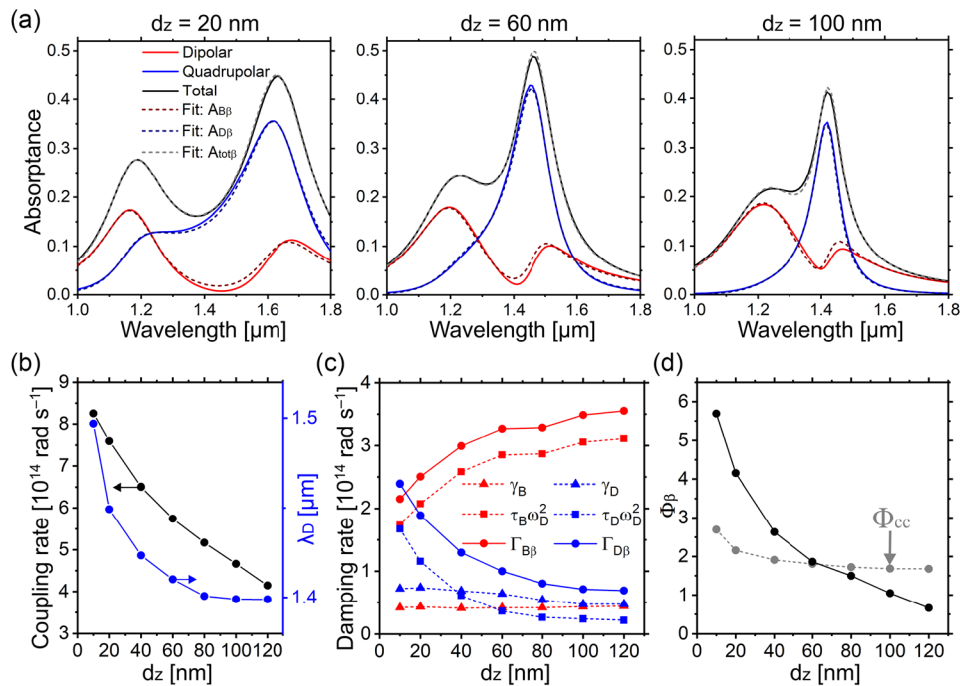


**Figure 5.** a)  $A_{B\beta}$ ,  $A_{D\beta}$ , and  $A_{\text{tot}\beta}$  fitted to the absorption spectra of the dipolar antenna, the quadrupolar antenna, and the DQA, respectively. The absorption spectra of the dipolar antenna, the quadrupolar antenna, and the DQA are taken from Figure 4b.  $A_{B\beta}$ ,  $A_{D\beta}$ , and  $A_{\text{tot}\beta}$  are calculated using the ECO model (Equation (11)). b) The black and blue marks are the fitting values of the coupling rate and the resonance wavelength of the quadrupolar antenna, respectively. c) The red and blue marks are the fitting values of damping rates of the dipolar and quadrupolar antennas, respectively. The triangle, square, and circle marks are the intrinsic, radiative, and total damping rates, respectively. The total damping rates are calculated by  $\Gamma_{n\beta} = \gamma_n + \tau_n \omega_D^2$ . d) The black and gray marks show  $\Phi_\beta$  and  $\Phi_{cc}$ , respectively. Those are calculated using the fitting values in (b) and (c).

are shown in Figure 5d as a function of  $d_z$ . When  $d_z = 60$  nm, the critical coupling  $\Phi_\beta = \Phi_{cc}$  is nearly satisfied. In Figure 4b, it can be found that the absorption of the quadrupolar antenna is maximized at  $d_z = 60$  nm. Therefore, these findings prove that  $\Phi_\beta$  and  $\Phi_{cc}$  can be indicators to achieve the maximum absorption of the quadrupolar antenna. Furthermore, from  $\Phi_\beta$  and  $\Phi_{cc}$ , we can understand the coupling regime of the DQA. In the case of the PPA, the coupling is classified into the weak or the strong coupling regimes by checking whether  $\Phi_\alpha$  is smaller or larger than 1. However, in the case of DQA,  $\Phi_\beta$  has to be compared with  $\Phi_{cc}$ . The absorption of the quadrupolar antenna shown in Figure 4b has a sharp peak for  $\Phi_\beta < \Phi_{cc}$ , but it shows mode splitting for  $\Phi_\beta > \Phi_{cc}$ . Therefore, we can find that  $\Phi_\beta < \Phi_{cc}$  gives the weak coupling regime and  $\Phi_\beta > \Phi_{cc}$  gives the strong coupling regime. As the ECO models used for the PPA and the DQA are almost the same, it is intuitively understood that the absorption properties of the DQA are nearly identical to those of the PPA.

The  $d_y$  dependence of the absorption properties of the DQA was also investigated in a similar manner to the  $d_z$  dependency (S6, Supporting Information).  $A_{B\beta}$ ,  $A_{D\beta}$ , and  $A_{\text{tot}\beta}$  of Equation (11) also agree with the FEM simulation for the  $d_y$  dependency. Comparing the coupling rate for the  $d_y$  and  $d_z$  dependencies, it is found that two different sets of ( $d_y$ ,  $d_z$ ) can have a similar coupling rate. The DQA with those sets of ( $d_y$ ,  $d_z$ ) has almost the same absorption spectra. Therefore, we conclude that the absorption properties of the DQA are

determined by the coupling rate, which can be controlled by changing the position of the dipolar antenna in the  $y$ - $z$  plane.

Taubert et al. proposed a CO model including phase retardation in coupling to investigate the mechanism of EIA occurring in the DQA.<sup>[8a,b]</sup> They described that the phase retardation effect can make the coupling constructive, resulting in EIA. The absorption spectra obtained using the CO model with phase retardation agree with the absorption of the DQA. However, this agreement can only be seen for the total absorption of the DQA, but not for the individual absorption spectra of the dipolar and quadrupolar antennas (S7, Supporting Information). If the distance between the dipolar and quadrupolar antennas is comparable to the wavelength, their coupling occurs through their far-field. In this case, the coupling may contain distance-dependent retardation effects, which has been suggested by our previous work based on the coupled-dipole method.<sup>[7b]</sup> In case the gap distance of the DQA is much smaller than the wavelength (e.g., refs. [8a,b]), we expect that the near-field effect dominates the coupling phenomenon of the DQA. This indicates that retardation effects play a subordinate role in near-field coupled systems. Considering the facts discussed above, we conclude that the EIA in the DQA is not attributed to phase retardation, but its EIA originates from the absorption enhancement in the quadrupolar antenna. Note that our results just indicate that a phase-retarded coupling may not be an appropriate interpretation to explain the absorption properties of the DQA, but EIA by a

phase-retarded coupling may be observed in other plasmonic systems (S8, Supporting Information).<sup>[7b,11]</sup>

Before concluding this work, it is essential to discuss the potential influence of the environment around the plasmonic systems on EIA for transitioning into an experimental investigation. In our study, we optimized the environment to simplify our analysis. For example, we considered that the surrounding of the PPA has a refractive index of 1.46 to investigate the shell thickness dependency of the PPA's absorption. However, when the PPA is experimentally realized, the surrounding may have a refractive index different from 1.46. Also, in an experiment, it is expected that the PPA and DQA are fabricated on a substrate, but we did not include the substrate in our simulation models. These environmental parameters influence the optical properties of the plasmonic systems. However, it is expected that these parameters do not significantly impact EIA. Throughout our work, we demonstrated that the critical coupling governs EIA. The critical coupling can be achieved for different environments by optimizing the plasmonic systems with taking the environmental parameters into account. Therefore, it is possible to induce EIA in an experimental system.

#### 4. Conclusion

We theoretically investigated the absorption properties of the PPA and the DQA, which are widely known for plasmonic EIA. We find that in those coupled plasmonic systems, the absorption of the bright oscillator always splits into two peaks, and the absorption of the dark oscillator is enhanced at the resonance of the dark oscillator by near-field coupling. To gain a deeper understanding of the absorption enhancement in the dark oscillator, we introduced an ECO model, including radiative damping originated from the Abraham–Lorentz force. We demonstrated that our ECO model can quantitatively describe the absorption properties of those systems. Using the ECO model, we found two essential parameters to maximize the absorption of the dark oscillator. One is the degree of coupling  $\Phi$ .  $\Phi$  is determined solely by the ratio between the coupling rate and the total damping rate of the whole system. Another parameter is the critical coupling state  $\Phi_{cc}$ , which is equal to 1 when the resonances of the bright and dark oscillators are aligned. When  $\Phi$  is equal to  $\Phi_{cc}$ , the critical coupling occurs, resulting in a maximum absorption of the dark oscillator. Our ECO model predicted that the absorption of the dark oscillator can be enhanced up to 25% of the maximum extinction of the bright oscillator without coupling.

Maximizing the absorption of the dark resonator, however, is not sufficient to observe EIA-like spectra. In addition, the bright oscillator should have a radiative damping sufficiently larger than its intrinsic one so that the absorption of the bright oscillator can be smaller than that of the dark oscillator. By doing this, the sharp absorption peak of the dark oscillator can be visible in a total absorption spectrum of a whole system, resulting in an EIA-like spectral profile. Notably, the absorption of the dark oscillator is independent of the ratio between intrinsic and radiative damping of the bright oscillator. Therefore, if plasmonic EIA is dominated by the maximization of the dark oscillator's absorption, plasmonic EIA is determined just by  $\Phi$  and  $\Phi_{cc}$ .

This interpretation of plasmonic EIA can be applied to many plasmonic systems similar to the PPA and the DQA.

Using our ECO model, we developed a new interpretation of plasmonic EIA, which is essential to advance EIA-based plasmonic systems. In addition, our ECO model may be able to provide details about Rabi splitting and energy transfer, which play a crucial role in plasmon–exciton coupled systems<sup>[19b,30]</sup> and surface-enhanced infrared absorption spectroscopies.<sup>[31]</sup> Therefore, we expect that this work can be beneficial for a wide range of applications and may outline an approach to develop a new type of plasmonic system.

#### Supporting Information

Supporting Information is available from the Wiley Online Library or from the author.

#### Acknowledgements

This project was funded by the European Research Council (ERC) under the European Union's Horizon 2020 research and innovation program (grant agreement no. 714968).

Open Access funding enabled and organized by Projekt DEAL.

#### Conflict of Interest

The authors declare no conflict of interest.

#### Data Availability Statement

The data that support the findings of this study are available from the corresponding author upon reasonable request.

#### Keywords

electromagnetically induced absorption (EIA), electromagnetically induced transparency (EIT), light absorption, near-field coupling, plasmonics

Received: July 18, 2022

Revised: March 1, 2023

Published online: April 3, 2023

- [1] a) B. Gallinet, O. J. F. Martin, *Phys. Rev. B* **2011**, *83*, 235427; b) B. Gallinet, O. J. Martin, *ACS Nano* **2011**, *5*, 8999; c) B. Peng, S. K. Ozdemir, W. Chen, F. Nori, L. Yang, *Nat. Commun.* **2014**, *5*, 5082; d) M. F. Limonov, M. V. Rybin, A. N. Poddubny, Y. S. Kivshar, *Nat. Photonics* **2017**, *11*, 543; e) J. A. Fauchaux, J. Fu, P. K. Jain, *J. Phys. Chem. C* **2014**, *118*, 2710.
- [2] a) C. L. Garrido Alzar, M. A. G. Martinez, P. Nussenzeig, *Am. J. Phys.* **2002**, *70*, 37; b) N. Liu, L. Langguth, T. Weiss, J. Kastel, M. Fleischhauer, T. Pfau, H. Giessen, *Nat. Mater.* **2009**, *8*, 758; c) R. Adato, A. Artar, S. Erramilli, H. Altug, *Nano Lett.* **2013**, *13*, 2584; d) P. Tassin, L. Zhang, R. Zhao, A. Jain, T. Koschny, C. M. Soukoulis, *Phys. Rev. Lett.* **2012**, *109*, 187401; e) P. Tassin, L. Zhang, T. Koschny, E. N. Economou, C. M. Soukoulis, *Phys. Rev. Lett.* **2009**, *102*, 053901.
- [3] S. Zhang, D. A. Genov, Y. Wang, M. Liu, X. Zhang, *Phys. Rev. Lett.* **2008**, *101*, 047401.

- [4] C. Ma, Y. Zhang, Y. Zhang, S. Bao, J. Jin, M. Li, D. Li, Y. Liu, Y. Xu, *Nanoscale Adv.* **2021**, *3*, 5636.
- [5] B. Metzger, T. Schumacher, M. Hentschel, M. Lippitz, H. Giessen, *ACS Photonics* **2014**, *1*, 471.
- [6] a) N. Liu, T. Weiss, M. Mesch, L. Langguth, U. Eigenthaler, M. Hirscher, C. Sonnichsen, H. Giessen, *Nano Lett.* **2010**, *10*, 1103; b) J. B. Lassiter, H. Sobhani, J. A. Fan, J. Kundu, F. Capasso, P. Nordlander, N. J. Halas, *Nano Lett.* **2010**, *10*, 3184.
- [7] a) J. Li, R. Gan, Q. Guo, H. Liu, J. Xu, F. Yi, *Opt. Express* **2018**, *26*, 16769; b) K. Matsumori, R. Fujimura, M. Retsch, *Opt. Express* **2022**, *30*, 14258.
- [8] a) R. Taubert, M. Hentschel, J. Kastel, H. Giessen, *Nano Lett.* **2012**, *12*, 1367; b) R. Taubert, M. Hentschel, H. Giessen, *J. Opt. Soc. Am. B* **2013**, *30*, 3123; c) J. He, P. Ding, J. Wang, C. Fan, E. Liang, *Opt. Express* **2015**, *23*, 6083.
- [9] a) T. Zhang, J. Dai, Y. Dai, Y. Fan, X. Han, J. Li, F. Yin, Y. Zhou, K. Xu, *Opt. Express* **2017**, *25*, 26221; b) W. Xiong, W. Wang, F. Ling, W. Yu, J. Yao, *AIP Adv.* **2019**, *9*, 115314.
- [10] J. Krauth, T. Schumacher, J. Defrance, B. Metzger, M. Lippitz, T. Weiss, H. Giessen, M. Hentschel, *ACS Photonics* **2019**, *6*, 2850.
- [11] D. Floess, M. Hentschel, T. Weiss, H.-U. Habermeier, J. Jiao, S. G. Tikhodeev, H. Giessen, *Phys. Rev. X* **2017**, *7*, 021048.
- [12] a) C. Wu, B. Neuner, G. Shvets, J. John, A. Milder, B. Zollars, S. Savoy, *Phys. Rev. B* **2011**, *84*, 075102; b) S. Tret'yakov, *Plasmonics* **2014**, *9*, 935.
- [13] T. Neuman, C. Huck, J. Vogt, F. Neubrech, R. Hillenbrand, J. Aizpurua, A. Pucci, *J. Phys. Chem. C* **2015**, *119*, 26652.
- [14] F. Zhang, X. Huang, W. Cai, R. Yang, Q. Fu, Y. Fan, Y. Hu, K. Qiu, W. Zhang, C. Li, Q. Li, *Opt. Express* **2020**, *28*, 17481.
- [15] a) X. Zhang, N. Xu, K. Qu, Z. Tian, R. Singh, J. Han, G. S. Agarwal, W. Zhang, *Sci. Rep.* **2015**, *5*, 10737; b) X. Hu, S. Yuan, A. Armghan, Y. Liu, Z. Jiao, H. Lv, C. Zeng, Y. Huang, Q. Huang, Y. Wang, J. Xia, *J. Phys. D: Appl. Phys.* **2017**, *50*, 025301; c) R. Yahiaoui, J. A. Burrow, S. M. Mekonen, A. Sarangan, J. Mathews, I. Agha, T. A. Searles, *Phys. Rev. B* **2018**, *97*, 155403; d) S. Lee, Q. H. Park, *Sci. Rep.* **2016**, *6*, 21989; e) A. Lovera, B. Gallinet, P. Nordlander, O. J. F. Martin, *ACS Nano* **2013**, *7*, 4527; f) A. Gandman, R. T. Mackin, B. Cohn, I. V. Rubtsov, L. Chuntonov, *ACS Nano* **2018**, *12*, 4521.
- [16] a) M. A. Kats, N. Yu, P. Genevet, Z. Gaburro, F. Capasso, *Opt. Express* **2011**, *19*, 21748; b) Z. Pan, J. Guo, *Opt. Express* **2013**, *21*, 32491.
- [17] K. S. Lee, M. A. El-Sayed, *J. Phys. Chem. B* **2005**, *109*, 20331.
- [18] a) K. Chen, R. Adato, H. Altug, *ACS Nano* **2012**, *6*, 7998; b) B. Cohn, K. Das, A. Basu, L. Chuntonov, *J. Phys. Chem. Lett.* **2021**, *12*, 7060.
- [19] a) H. Chen, L. Shao, K. C. Woo, J. Wang, H.-Q. Lin, *J. Phys. Chem. C* **2012**, *116*, 14088; b) T. J. Antosiewicz, S. P. Apell, T. Shegai, *ACS Photonics* **2014**, *1*, 454.
- [20] S. Babar, J. H. Weaver, *Appl. Opt.* **2015**, *54*, 477.
- [21] X. Zhang, J. Qiu, J. Zhao, X. Li, L. Liu, *J. Quant. Spectrosc. Radiat. Transf.* **2020**, *252*, 107063.
- [22] a) H. Luo, Z. Kang, Y. Gao, H. Peng, J. Li, G. Qin, Y. Liu, *Opt. Express* **2019**, *27*, 4886; b) N. Li, H. Yin, X. Zhuo, B. Yang, X.-M. Zhu, J. Wang, *Adv. Opt. Mater.* **2018**, *6*, 1800436; c) M. Mayer, L. Scarabelli, K. March, T. Altantzis, M. Tebbe, M. Kociak, S. Bals, F. J. Garcia de Abajo, A. Fery, L. M. Liz-Marzan, *Nano Lett.* **2015**, *15*, 5427; d) D. Huo, M. J. Kim, Z. Lyu, Y. Shi, B. J. Wiley, Y. Xia, *Chem. Rev.* **2019**, *119*, 8972.
- [23] N. Murata, R. Hata, H. Ishihara, *J. Phys. Chem. C* **2015**, *119*, 25493.
- [24] B. Gallinet, T. Siegfried, H. Sigg, P. Nordlander, O. J. Martin, *Nano Lett.* **2013**, *13*, 497.
- [25] C. Deeb, X. Zhou, J. Plain, G. P. Wiederrecht, R. Bachelot, M. Russell, P. K. Jain, *J. Phys. Chem. C* **2013**, *117*, 10669.
- [26] F. Stete, P. Schoßau, M. Bargheer, W. Koopman, *J. Phys. Chem. C* **2018**, *122*, 17976.
- [27] F. Stete, W. Koopman, M. Bargheer, *ACS Photonics* **2017**, *4*, 1669.
- [28] G. Zengin, G. Johansson, P. Johansson, T. J. Antosiewicz, M. Kall, T. Shegai, *Sci. Rep.* **2013**, *3*, 3074.
- [29] A. D. Rakic, A. B. Djuricic, J. M. Elazar, M. L. Majewski, *Appl. Opt.* **1998**, *37*, 5271.
- [30] a) A. E. Schlather, N. Large, A. S. Urban, P. Nordlander, N. J. Halas, *Nano Lett.* **2013**, *13*, 3281; b) G. P. Wiederrecht, G. A. Wurtz, J. Hranisavljevic, *Nano Lett.* **2004**, *4*, 2121.
- [31] F. Neubrech, C. Huck, K. Weber, A. Pucci, H. Giessen, *Chem. Rev.* **2017**, *117*, 5110.